ISAS RESEARCH NOTE

ISAS RN 668

X-ray calibration of the telescopes on board ASTRO-E satellite

R. Shibata, M. Ishida, H. Honda, T. Endo, J. Ishida,
H. Kunieda, Y. Tawara, A. Furuzawa, Y. Ogasaka,
M. Watanabe, K. Misakai, T. Yoshioka, P. J. Serlemitsos,
Y. Soong, K.-W. Chan, Y. Terashima, and S. Akao

THE INSTITUTE OF SPACE AND ASTRONAUTICAL SCIENCE

X-ray calibration of the telescopes on board ASTRO-E satellite

R. Shibata, M. Ishida, H. Honda, T. Endo, J. Ishida,

Institute of Space and Astronautical Science, 3-1-1 Yoshinodai, Sagamihara, Kanagawa, 229-8510, Japan

H. Kunieda, Y. Tawara, A. Furuzawa, Y. Ogasaka,
M. Watanabe, K. Misakai, T. Yoshioka,

Department of Astrophysics, Faculty of Science, Nagoya University Furo-cho, Chikusa, Nagoya, Aichi, 464-8602, Japan

P. J. Serlemitsos, Y. Soong, K.-W. Chan, Y. Terashima,

NASA Goddard Space Flight Center, Greenbelt, MD 20771

S. Akao

Graduate School of Cultural Studies and Human Science, Kobe University, 3-11, Tsurukabuto, Nada, Kobe, 657-8501, Japan

1. INTRODUCTION

ASTRO-E is an X-ray astronomy satellite which will be launched in February 2000 from Kagoshima Space Center, Japan. It carries five X-ray telescope (XRT) modules which adopt a thin foil-nesting Wolter Type-I optics as in the case of ASCA. The detectors, which are placed in the focal plane, are four X-ray Imaging Spectrometers (XIS), which adopt X-ray CCD cameras, and one X-Ray Spectrometer (XRS), which is the micro-calorimeter.

At the end of this century, three major X-ray astronomy satellites including ASTRO-E will be launched successively. AXAF (NASA) and XMM (ESA) will be in orbit in 1998 and 1999, respectively [1] [2]. All these satellites are equipped with the XRTs utilizing Wolter Type-I optics. In Fig. 1, we show the effective area of these satellites. XMM is equipped with three telescopes

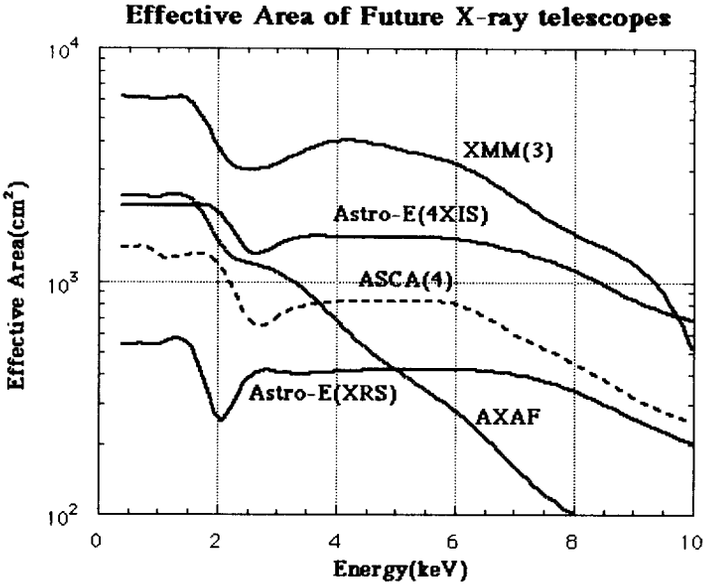

Figure 1. Total effective areas of the satellites which will be launched toward the end of this century. The effective area of ASCA is also shown for comparison.

and has the largest effective area, nearly three times and twice as large as that of ASTRO-E XIS at 1 keV and 6 keV, respectively. For two out of the three XRT modules of XMM, however, a grating system is inserted, and hence the total effective area is reduced to $\sim$ 60 % from Fig. 1[3] above 6 keV. Hence the effective area of ASTRO-E XIS is nearly comparable with that of XMM above 6 keV, in which the astrophysically important iron K emission line exists.

In this paper, we report the status of the pre-flight calibration of the ASTRO-E XRT which is being conducted at the Institute of Space and Astronautical Science (ISAS), Japan. In § 2, we describe the XRT designs and the technique of reflector production. In § 3, we explain the X-ray beam facility used for the pre-flight calibration. Results of the calibration are reported in § 4. A summary and conclusions are given in § 5.

Table 1. X-Ray Telescope Parameters

	ASTRO-E XIS (XRT–I)	ASTRO-E XRS (XRT–S)	ASCA
Number of Telescope	4	1	4
Focal Length	4750 mm	4500 mm	3500 mm
Plate Scale	0.73 ′/mm	0.76 ′/mm	0.98 ′/mm
Number of Nestings	175	168	120
Reflectors/Telescope	1400	1344	960
Primary incident angle	0.18° – 0.60°	0.19° – 0.63°	0.24° – 0.70°
Weight	18.0 kg	18.0 kg	9.84 kg
Reflector Substrate			
Material	Aluminum	Aluminum	Aluminum
Thickness	155 μm	155 μm	127 μm
Length	101.6 mm	101.6 mm	100 mm
Reflecting Surface			
Material	Au	Pt	Au
Thickness	> 1000 Å	> 1000 Å	500 Å
Other structure	Epoxy coupling layer 13 μm	Epoxy coupling layer 13 μm	Acrylic lacquer finish 10 μm
Housing			
Inner Diameter	118 mm	119 mm	120 mm
Outer Diameter	399 mm	400 mm	345 mm
Height†	225 mm	225 mm	218 mm
Geometric Area	873 cm^2	887 cm^2	558 cm^2
Effective Area			
@ 1.5keV	460 cm^2	460 cm^2	300cm^2
@ 8.0keV	250 cm^2	250 cm^2	100cm^2
Spatial Resolution			
(HPD††)	1.5 ′	1.5 ′	3.4 ′
Field of View			
@ 1.5 keV	20 ′	20 ′	24 ′
@ 8.0 keV	15 ′	15 ′	16 ′

† : Primary + Secondary

†† : Half Power Diameter

2.2. Production of Reflectors

Each reflector of the ASTRO-E XRTs is made by a replication technique developed at NASA/GSFC [5] [6]. Aluminum substrates are curved into the designed conical shape using a mechanical rolling. Then they are tightly pushed on a conical mold by the atmospheric pressure, and are baked at 140°C for 6 hours before replication. These are the procedure of the pre-forming of the substrates. On the other hand, more than 1000 Å of gold or platinum is deposited by the vacuum

3. ISAS X-RAY BEAM FACILITY

Pre-flight calibration of the ASTRO-E XRTs has been going on in the X-ray beam facility in ISAS. In Fig. 4, we show the outlook of the ISAS X-ray beamline. The length of the entire evacuated tube is about 36 m, the inner diameter of which is typically 32 cm. An X-ray generator is located at one end of the tube, and the telescope and detectors are placed at the other end in the "sample chamber" and the "detector chamber," respectively. The coordinate

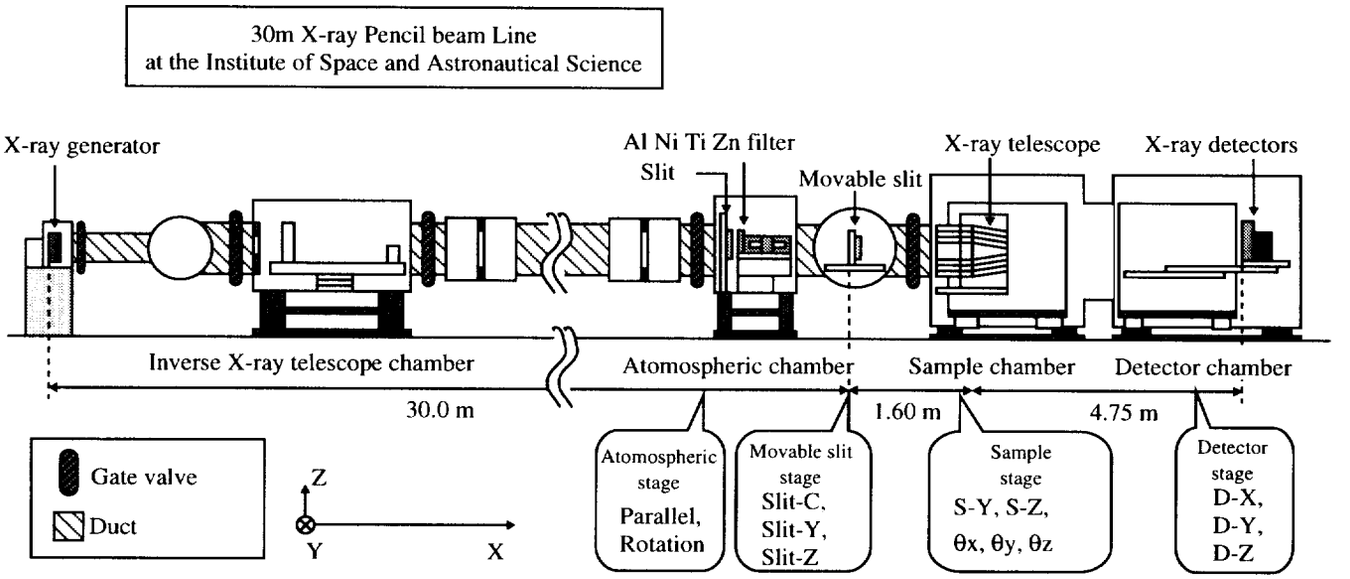

Figure 4. Outlook of the ISAS 30 m X-ray beamline

system is defined as follows: X-axis corresponds to the direction of the X-ray beam; Z-axis points upward; Y-axis is in the horizontal plane, perpendicular to both X and Z, forming a right-hand-coordinate system with them. In the following subsections, we explain components of our beamline in detail. Characteristics of each component are summarized in table 2.

3.1. X-ray Generator

The X-ray generator (RIGAKU RU-200) is equipped with a water-cooled rotary type X-ray target. Seed electrons are emitted from a thermally heated W-filament with the size of 1 × 10 mm^2. The electrons are accelerated by a high bias voltage (5–20 kV), and finally hit target metals. The electrons hitting the targets are loosing their kinetic energy by the bremsstrahlung, line X-ray emissions characteristic to the target metals, and the heat. The surface of the target is tilted by 6° with respect to the beam direction. Hence the effective filament size looked at from the downstream side of X-rays is 1×1 mm^2. Currently we can choose Al, Ti, Cu and Pt as target metals, whose emission line appears at 1.49 keV (Kα), 4.51 keV (Kα), 8.04 keV (Kα), and 9.40 keV (Lα), respectively. A high rotation rate (6000 rpm) of the target and a water-cooling system enable us to obtain a high surface brightness of X-rays.

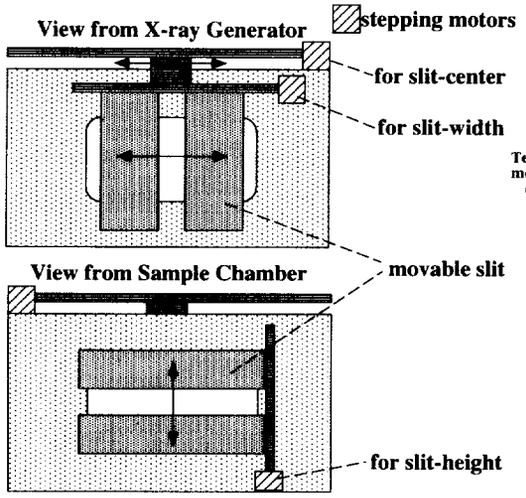

Figure 5. Schematic view of the movable slit. It can collimate the beam as small as 0.2 and 0.5 mm in Y and Z direction, and change the center of the beam in Y direction.

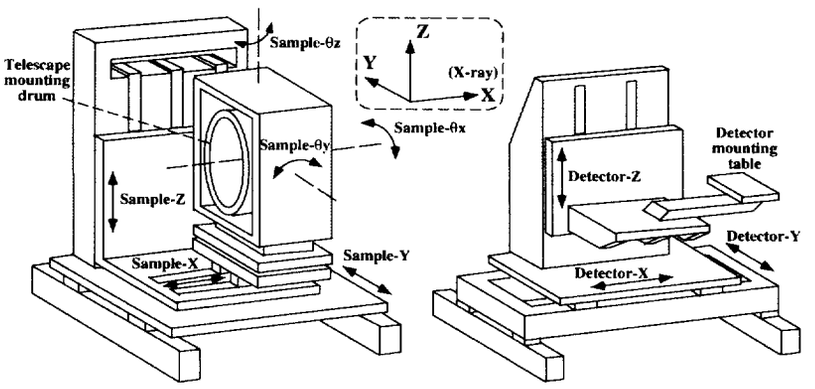

Figure 6. Specification of the mechanical stages in the sample (left) and the detector (right) chambers

3.3. Mechanical Stages

In order to fully illuminate the XRT with the narrow X-ray beam described above, we need to move the XRT in the evacuated sample chamber. Note that the detector should move simultaneously with the XRT for collecting the reflected photons. For this purpose, we have mechanical stages in both the sample and the detector chambers.

In Fig. 6, we show schematic views of the mechanical stages in the sample and detector chambers. The stroke of each stage is summarized in table 2. Both stages can move in the Y and Z directions. The detector stage can also move in the X direction to adjust the distance between the XRT and the detectors. The X stage in the sample chamber is moved manually. Its stroke, 25mm, corresponds to the difference between the focal lengths of the XRT–I and the XRT–S. In addition, we have triaxial rotational stages for the sample chamber stage. Among them, the rotational stages around the Y and the Z axes (hereafter referred to as θ_Y and θ_Z stages, respectively) are used for off-axis measurements.

3.4. Focal Plane Detectors

Two kinds of detectors, proportional counter (PC) and charge coupled device (CCD), are currently available in the ISAS X-ray beamline.

3.4.1. Proportional Counter

The proportional counter is operated by flowing P10 gas (90 % argon and 10 % methane) at 1 atm. The entrance window is a circle with 12 mmϕ covered with the aluminum-coated Mylar film with a thickness of 15 μm. We use a tungsten wire with 50 μmϕ for the anode. The depth of the gas measured from the entrance window is 22 mm. Note that PC has no imaging capability, and is mainly used to measure the total effective area of the XRT.

4. RESULTS OF PRE-FLIGHT CALIBRATIONS

In this section, we describe first results from the pre-flight calibration of the XRT–I carried out in the ISAS beamline. We have measured the effective area, the imaging capability, and the stray light at the energies of Kα lines of Al (1.49 keV), Ti (4.51 keV), and Cu (8.04 keV). As recognized from the designed effective area (Fig. 9), there is a huge discontinuity in the effective area at $\sim$ 2.2 keV. which corresponds to gold M shell (Au-M) absorption edge. The X-ray energies of Al-Kα (1.49 keV) and Ti-Kα (4.51 keV) are of great use in calibrating this discontinuity. On the other hand, Cu-Kα emission line (8.04 keV) is important in providing a data point in the energy range where the effective area decreases steeply with increasing X-ray energy.

4.1. Measurements of the Effective Area and the Imaging Capability

As mentioned in §§ 3.2, we collimate the intrinsic X-ray to obtain a highly parallel X-ray beam. In order to fully illuminate the XRT, we adopt the raster scan method: The sample Y stage and the detector Y stage (hereafter referred to as S_Y and D_Y stages, the same for the Z stages) are moved simultaneously from one edge of the XRT to the other. The detector collects reflected X-ray photons during this simultaneous Y scan. After this Y scan is finished, S_Z and D_Z stages are operated to shift both XRT and the detector by the beam width in Z direction. Then, S_Y and D_Y stages move in the opposite direction. These processes are repeated until the entire XRT face is illuminated.

In the case of using CCD, we use an X-ray beam size of 2 $\times$ 2 mm^2 in Y and Z with the movable slit. In this case, the full beam diverging angle is 13″ (eq.(1)). On the other hand, the PC has no imaging capability and hence a larger beam size is allowable. We thus expand the size of the beam in Z direction to be 4 mm, which makes the time necessary for the full scan shorter.

In Fig. 8, we show the brightness distribution of the X-ray beam of Cu (8.04 keV) in the case of 2$\times$2 mm^2 (for CCD). After removing Poissonic noise, the brightness distribution is flat within

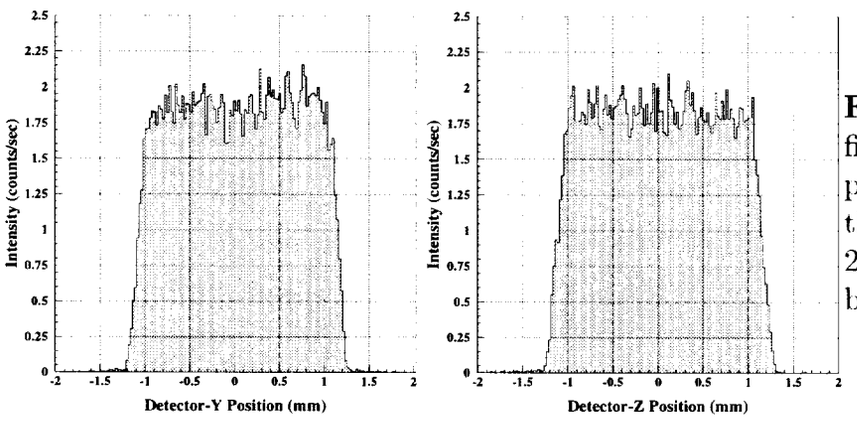

Figure 8. The X-ray beam profile with the size of 2 $\times$ 2 mm^2 projected on Y and Z axes. Note that the beam size is larger than 2 mm at the detector position because of the divergence.

a few percent. In order to use the CCD in the flux mode, it is important to make monochromatic X-ray beams. For this, we basically use a metal filter appropriate for each target. In table 4,

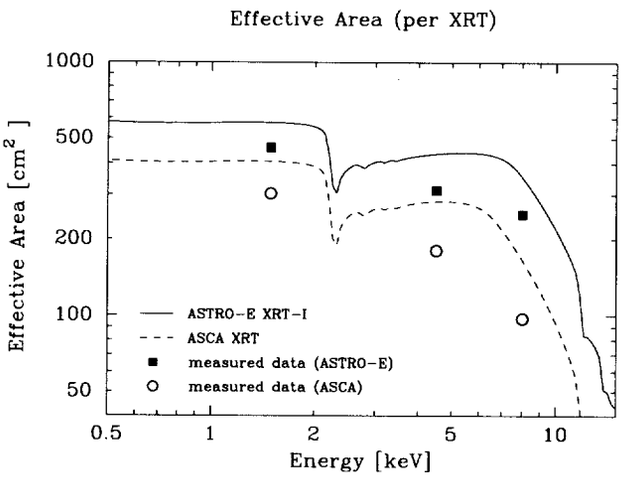

Figure 9. On-axis effective area of each XRT–I and ASCA XRT against X-ray energy. Marks are measured values, and the curves are the ideal effective areas calculated based on the XRT design parameters. The sharp drop at about 2.2 keV is attributed to the gold M-edge complex.

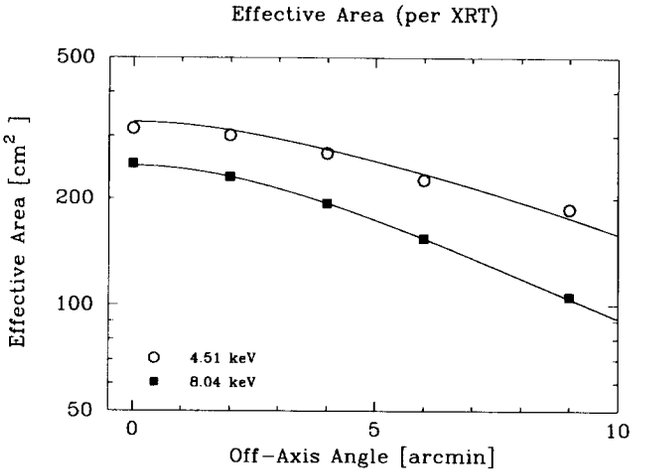

Figure 10. Angular response of the effective area at 4.51 and 8.04 keV. The effective area gradually decreases with the off-axis incidence because of neighboring reflectors shadowing and the increase of the average incident angles (vignetting). Curves are empirical model functions (double Gaussian). Marks are measured values.

XRT values are also shown. The ideal effective area assumes that the reflector has no surface roughness and that the placement of the reflectors is perfect. From this figure, it is recognized that the measured values of both XRT–I and ASCA are $\sim$ 75–80 % of ideal effective areas. In a separate experiment, we measured the reflectivity of each reflector and found that it is close to the ideal. Therefore, we consider that the smaller effective area is probably due to a slight misalignment of the reflectors. The measured effective areas of XRT–I are larger than the ASCA XRT by a factor of 1.5 and 2.5 at 1.49 and 8.04 keV, respectively.

The effective area is a function of the incident X-ray angles as well as the incident X-ray energy. Figure 10 shows the angular response of the effective area at X-ray energies, 4.51 and 8.04 keV. The abscissa indicates the "off-axis angle" which is the angle between the directions of incident X-rays and the XRT optical axis (= symmetry axis). One of the appropriate empirical models for the angular response is found to be a two Gaussian model, which is also drawn in the figure. The effective area drops with the off-axis angle because the neighboring reflectors prevent X-rays passing through and the reflectivity decreases more sensitively to the off-axis angle in higher X-ray energies. This is the so-called "vignetting effect." The field of view of the XRT–I, which we define to be the off-axis angle at which the effective area becomes half of the on-axis value, is $20'\phi$ and $15'\phi$ at 4.51 and 8.04 keV, respectively.

4.3. Image quality

The image quality of the XRT–I has been measured by the raster scan method using the CCD with a 2 $\times$ 2 mm^2 X-ray beam (13 arcsec beam divergence). Currently the measurement has

and conventionally is used as one of the quantitative expressions of the imaging capability. HPD of the XRT–I is obtained to be 1.84±0.04 arcmin, which is two times better than the ASCA XRT. Note that the normalized radii of EEFs are 4.5 arcmin and 6.0 arcmin, respectively, for the XRT–I and the ASCA XRT because we use the same CCD for both in spite of the difference of the focal lengths (4750mm and 3500mm: see the plate scale in table 1).

4.4. Stray Light

Because of the thin reflector-nesting configuration of the XRT, it is possible that X-rays intrude from outside the field of view (FOV). In Fig. 13, we show patterns of the stray lights. The

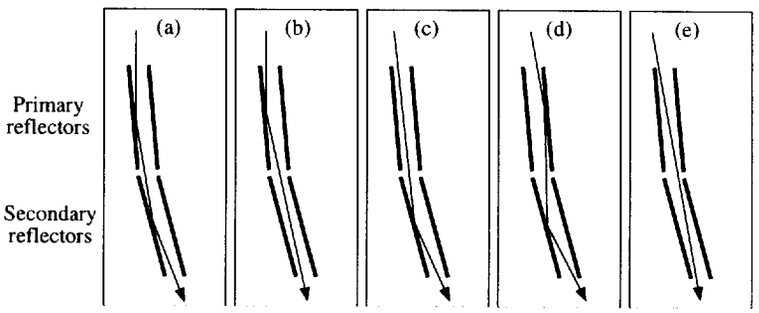

Figure 13. Four examples of XRT light paths: (a) normal path, (b) reflection only by primary reflectors, (c) reflection only by secondary reflectors, (d) multiple reflections by front and back surface of reflectors, (e) direct path (no reflection).

normal light path is (a), and the others are the stray lights. They are classified as (b) primary reflection, (c) secondary reflection, (d) multiple reflection, and (e) no reflection. Among them the multiple reflection is expected to have an energy dependence, because it includes reflection at the backside of the reflector which is bare aluminum. The multiple reflection is thus expected to be more intense for lower X-ray energies.

Since the stray lights spread widely over the focal plane, we have performed a mosaic mapping with the CCD. We set a sector of the XRT-I horizontally, and performed a one dimensional scan in Y direction with 2×2 mm^2 X-ray beam, simultaneously with the S_Y and the D_Y stages. In this configuration, the stray lights spread in the Y direction. Therefore, the CCD was moved in this direction with the D_Y stage for the mosaic mapping. The stray lights were measured at offset angles of 0.5° and 1.0° The XRT is rotated around the Z axis by these values by using θ_Z stage. The stray lights were measured at the X-ray energies of 1.49, 4.51 and 8.04 keV.

Figure 14 displays the one dimensional brightness distribution of the stray lights with the offset angle of 0.5° (panel (I), (II), and (III)) and 1.0° (panel (IV) and (V)). The ordinates are the brightness (counts s^{-1} mm^{-2}) in the focal plane in the case when the X-ray star with the on-axis intensity of 1 count s^{-1} is the source of the stray lights. Note that the on-axis position of the XRT–I is 30′ in the abscissa for the upper three panels, and 60′ for the lower two panels.

As noticed from this figure, the on-axis position (at which the detector locates in orbit) is contaminated by two components of the stray light, (c) secondary reflection and (d) multiple reflection. As expected, the multiple reflection component decreases with increasing X-ray energy, and becomes almost negligible at Cu-Kα and Ti-Kα energies (8.04 keV and 4.51 keV) for the off-axis angles of 0.5° and 1.0°, respectively. Note that the peak brightness of the stray light at Al-Kα (1.49 keV) is only 2×10^{-5} counts s^{-1} mm^{-2} (component (c)), which is almost

with a length scale of several tens down to several mm, and the small scattering tail was brought about by reduction of the surface roughness with scale down to several μm.

The brightness of the stray light was obtained to be less than 2×10^{-5} counts s^{-1} mm^{-2} in the case when an X-ray star with the on-axis intensity of 1 count s^{-1} is the source of the stray lights. This peak brightness is caused by the secondary reflection, and hence it is almost the same as ASCA. However, the brightness of the multiple reflection component is remarkably smaller than ASCA, at least by several factors. This is the result because the backside of the reflector of ASTRO-E XRT is a bare aluminum; but it was coated by acrylic lacquer in the ASCA XRT.

REFERENCES

1. M. C. Weisskopf, S. L. O'Dell, R. F. Elsner, and L. P. Van Speybroeck, *Proc. SPIE*, **2515**, pp.312-329, 1995.

2. D. H. Lumb, H. Eggel, R. Lainé, and A. J. Peacock, *Proc. SPIE*, **2808**, pp.326-337, 1996.

3. J. v. Casteren, *Proc. SPIE*, **2808**, pp.338-349, 1996.

4. P. Serlemitsos et al, *Publication of Astronomical Society of Japan*, **47**, pp.105-114, 1995.

5. Y. Soong et al, *Proc. SPIE*, **2515**, pp.64-69, 1995.

6. P. Serlemitsos et al, *Astrophysics & Space Astronomy*, **239**, pp.177-196, 1996.

X-ray calibration of the telescopes on board ASTRO-E satellite

R. Shibata, M. Ishida, H. Honda, T. Endo, J. Ishida,

Institute of Space and Astronautical Science, 3-1-1 Yoshinodai, Sagamihara, Kanagawa, 229-8510, Japan

H. Kunieda, Y. Tawara, A. Furuzawa, Y. Ogasaka,
M. Watanabe, K. Misakai, T. Yoshioka,

Department of Astrophysics, Faculty of Science, Nagoya University Furo-cho, Chikusa, Nagoya, Aichi, 464-8602, Japan

P. J. Serlemitsos, Y. Soong, K.-W. Chan, Y. Terashima,

NASA Goddard Space Flight Center, Greenbelt, MD 20771

S. Akao

Graduate School of Cultural Studies and Human Science, Kobe University, 3-11, Tsurukabuto, Nada, Kobe, 657-8501, Japan

ABSTRACT

We present the first results of pre-flight calibrations of the X-ray telescopes on board the ASTRO-E satellite. They adopt a thin foil-nesting Wolter Type-I optics, which is in principle the same as ASCA XRTs. Owing to a scale up of the telescope and a new technique of the reflector production, however, both the effective area and the imaging capability are improved. In the current measurements, the effective area is obtained to be 460, 313 and 250 cm^2 per XRT at 1.49, 4.51, and 8.04 keV, respectively, which is significantly larger than ASCA by a factor of 1.5 and 2.5 at 1.49 keV and 8.04 keV. The point spread function also shows a better focusing capability than ASCA by a factor of 2, and the half power diameter is obtained to be 1.84 arcmin at 4.51 keV. The brightness of the stray light is obtained to be $2\times\ 10^{-5}$ counts s^{-1} mm^{-2} at the brightest part of the stray light image, in the case when the X-ray star with the on-axis intensity of 1 count s^{-1} is the source of the stray lights, which is almost the same with ASCA.

Keywords: X-ray telescope, effective area, point spread function, half power diameter, ASTRO-E

1. INTRODUCTION

ASTRO-E is an X-ray astronomy satellite which will be launched in February 2000 from Kagoshima Space Center, Japan. It carries five X-ray telescope (XRT) modules which adopt a thin foil-nesting Wolter Type-I optics as in the case of ASCA. The detectors, which are placed in the focal plane, are four X-ray Imaging Spectrometers (XIS), which adopt X-ray CCD cameras, and one X-Ray Spectrometer (XRS), which is the micro-calorimeter.

At the end of this century, three major X-ray astronomy satellites including ASTRO-E will be launched successively. AXAF (NASA) and XMM (ESA) will be in orbit in 1998 and 1999, respectively [1] [2]. All these satellites are equipped with the XRTs utilizing Wolter Type-I optics. In Fig. 1, we show the effective area of these satellites. XMM is equipped with three telescopes

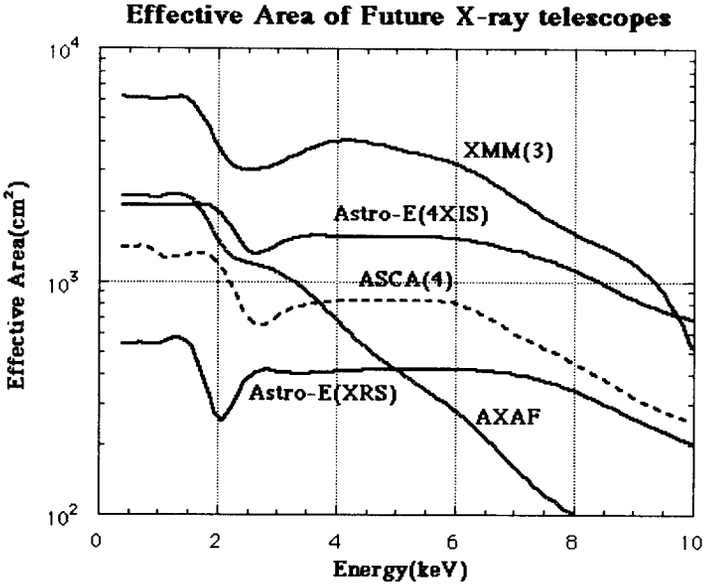

Figure 1. Total effective areas of the satellites which will be launched toward the end of this century. The effective area of ASCA is also shown for comparison.

and has the largest effective area, nearly three times and twice as large as that of ASTRO-E XIS at 1 keV and 6 keV, respectively. For two out of the three XRT modules of XMM, however, a grating system is inserted, and hence the total effective area is reduced to $\sim$ 60 % from Fig. 1[3] above 6 keV. Hence the effective area of ASTRO-E XIS is nearly comparable with that of XMM above 6 keV, in which the astrophysically important iron K emission line exists.

In this paper, we report the status of the pre-flight calibration of the ASTRO-E XRT which is being conducted at the Institute of Space and Astronautical Science (ISAS), Japan. In § 2, we describe the XRT designs and the technique of reflector production. In § 3, we explain the X-ray beam facility used for the pre-flight calibration. Results of the calibration are reported in § 4. A summary and conclusions are given in § 5.

2. STRUCTURE OF XRT AND PRODUCTION OF REFLECTORS

2.1. Structure of XRT

X-rays are easily absorbed by materials, and thus it is impossible to construct any normal incidence optics. Since the index of refraction is slightly less than unity, however, the total reflection of X-rays occurs if the X-rays are incident on a smooth, flat surface of matter almost tangentially. By making use of this property, we can make up so-called "grazing incidence optics. "

Among several kinds of grazing incidence optics, the Wolter Type-I optics has been commonly used for X-ray astronomy satellites so far in orbit. In this optics, the incident X-rays are reflected twice by a confocal paraboloid (primary) and a hyperboloid (secondary). The ASTRO-E XRT also adopts this optics in principle. Note, however, that the effective area becomes less than 1/50 of the geometrical area of the reflector because of the grazing incidence. To cope with this situation, one usually nests the pair of reflectors radially. In ASTRO-E, we nest the reflectors as many as possible by using a substrate as thin as possible in order to obtain a large effective area up to 10 keV. The thin substrate, however, prevents us from realizing paraboloids and hyperboloids for the reflectors. We thus substitute conical surfaces for both.

In table 1, we summarize the parameters of the XRTs on board ASTRO-E. For comparison, we also tabulated those from ASCA XRTs [4]. For ASTRO-E, we have two kinds of telescopes with different focal lengths. One is for the X-ray CCD cameras with $f = 4.75$ m (4 modules), and the other is for the X-ray micro-calorimeter with $f = 4.50$ m (1 module). Hereafter, they are referred to as "XRT–I" and "XRT–S," respectively. In ASTRO-E, as well as in ASCA, each XRT is composed of the equivalent four "quadrants." Each quadrant comprises a primary and a secondary housing which contain the reflectors for the primary and the secondary reflection. The numbers of reflectors per housing are 175 and 168, respectively, for the XRT–I and the XRT–S. Figure 2 is a picture of XRT–I, and Figure 3 is a drawing of one quadrant. The reflectors of each housing are supported by thirteen alignment bars, which are evenly spaced in azimuth, from both the top and the bottom sides. Each alignment bar has grooves to catch the reflectors, determining the positions of the reflectors as well as sustaining their shape. The four quadrants are connected by inner and outer rings from the top and the bottom sides, and are made into one full telescope.

Although ASTRO-E XRT is the same as ASCA XRT in principle, two kinds of improvements are made since ASCA: One is the improvement of the reflector production method — a replication technique — which is described in the next subsection in more detail, and the other is the scale up effect. Owing to a larger diameter of the XRT, the geometrical area of the reflectors increases by a factor of ~ 1.5, which brings about the increase of effective area by the same factor almost energy independently. In addition to this, a longer focal length makes the incident angles to the primary reflectors smaller (table 1). This contributes to a further increase of the effective area more in higher energies. As a result, the effective area becomes significantly larger than ASCA by a factor of 1.5 and 2.5 at the X-ray energy of 1.5 keV and 8.0 keV, respectively.

Table 1. X-Ray Telescope Parameters

	ASTRO-E XIS (XRT–I)	ASTRO-E XRS (XRT–S)	ASCA
Number of Telescope	4	1	4
Focal Length	4750 mm	4500 mm	3500 mm
Plate Scale	0.73 ′/mm	0.76 ′/mm	0.98 ′/mm
Number of Nestings	175	168	120
Reflectors/Telescope	1400	1344	960
Primary incident angle	0.18° – 0.60°	0.19° – 0.63°	0.24° – 0.70°
Weight	18.0 kg	18.0 kg	9.84 kg
Reflector Substrate			
Material	Aluminum	Aluminum	Aluminum
Thickness	155 μm	155 μm	127 μm
Length	101.6 mm	101.6 mm	100 mm
Reflecting Surface			
Material	Au	Pt	Au
Thickness	> 1000 Å	> 1000 Å	500 Å
Other structure	Epoxy coupling layer 13 μm	Epoxy coupling layer 13 μm	Acrylic lacquer finish 10 μm
Housing			
Inner Diameter	118 mm	119 mm	120 mm
Outer Diameter	399 mm	400 mm	345 mm
Height†	225 mm	225 mm	218 mm
Geometric Area	873 cm^2	887 cm^2	558 cm^2
Effective Area			
@ 1.5keV	460 cm^2	460 cm^2	300cm^2
@ 8.0keV	250 cm^2	250 cm^2	100cm^2
Spatial Resolution			
(HPD††)	1.5 ′	1.5 ′	3.4 ′
Field of View			
@ 1.5 keV	20 ′	20 ′	24 ′
@ 8.0 keV	15 ′	15 ′	16 ′

† : Primary + Secondary

†† : Half Power Diameter

2.2. Production of Reflectors

Each reflector of the ASTRO-E XRTs is made by a replication technique developed at NASA/GSFC [5] [6]. Aluminum substrates are curved into the designed conical shape using a mechanical rolling. Then they are tightly pushed on a conical mold by the atmospheric pressure, and are baked at 140°C for 6 hours before replication. These are the procedure of the pre-forming of the substrates. On the other hand, more than 1000 Å of gold or platinum is deposited by the vacuum

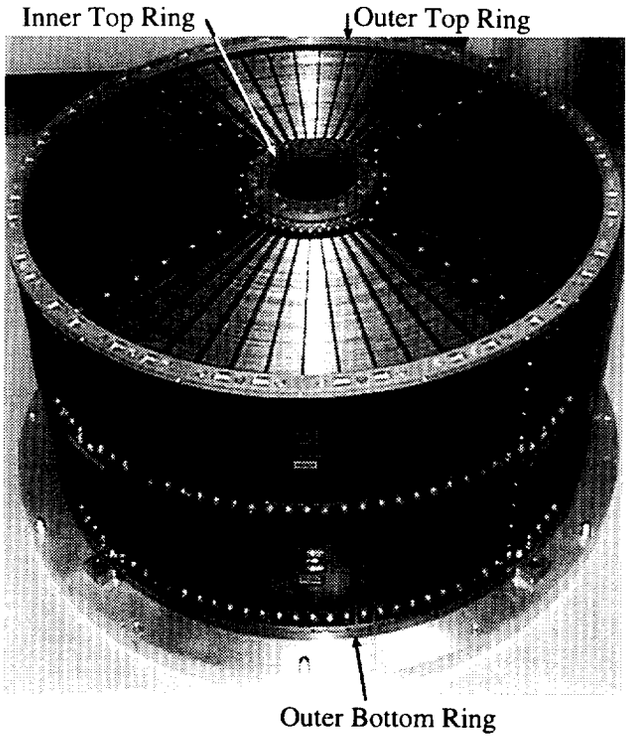

Figure 2. ASTRO-E XRT-I flight model (without thermal shield)

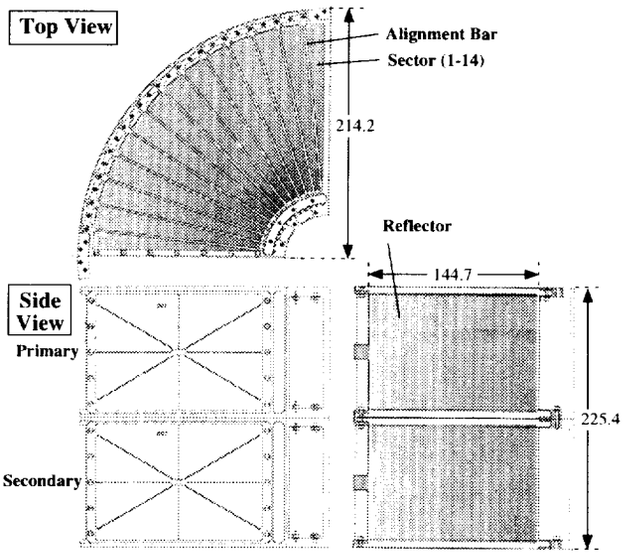

Figure 3. ASTRO-E XRT quadrant housing. 175 foil reflectors are installed in each of the two layers. Also shown are the 13 alignment bar which supported the reflectors in the housing.

evaporation on the conical glass mandrels whose surfaces are finely polished. The mandrels are produced for every ~10 substrates. The epoxy adhesive is sprayed gold (or platinum) on the mandrels and the substrates. Their faces are attached with each other in a vacuum chamber, and then baked at 40 °C for 8 hours. After this, the aluminum substrate is peeled off from the mandrel at the boundary between the glass and gold (or platinum), and finally made into a reflector.

The reflector made in the above method shows the performance which is superior to the ASCA XRT. The substrates of ASCA reflectors are dipped into an acrylic bath to smooth their surface after the pre-forming which is the same as for ASTRO-E, and gold is deposited by the vacuum evaporation.

Because the replication method can print the surface of the finely polished mandrel on the reflecting surface, reducing both the surface roughness of a few to a hundred μm scale and the surface undulation with a scale down to mm which are inherent to the substrate, the X-ray image quality is greatly improved (§§ 4.3). Also, the backside surface of the reflector is a raw aluminum, and is not smoothed by acrylic coating as in the case of ASCA XRT, which reduces the amount of the "stray light" remarkably.

3. ISAS X-RAY BEAM FACILITY

Pre-flight calibration of the ASTRO-E XRTs has been going on in the X-ray beam facility in ISAS. In Fig. 4, we show the outlook of the ISAS X-ray beamline. The length of the entire evacuated tube is about 36 m, the inner diameter of which is typically 32 cm. An X-ray generator is located at one end of the tube, and the telescope and detectors are placed at the other end in the "sample chamber" and the "detector chamber," respectively. The coordinate

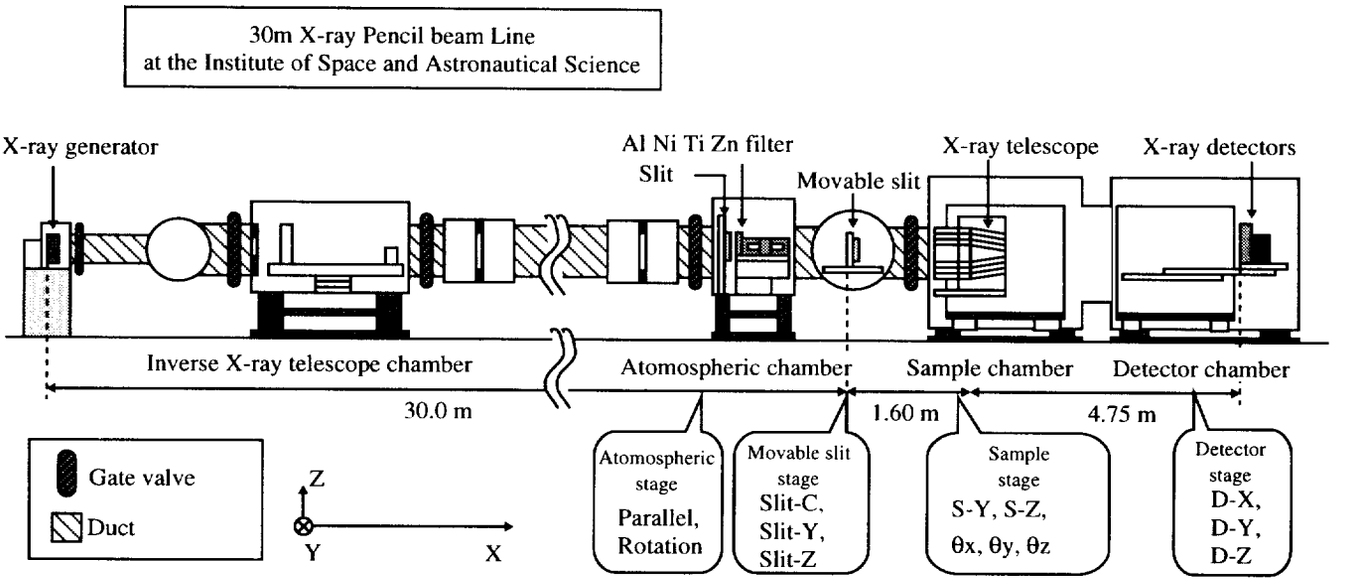

Figure 4. Outlook of the ISAS 30 m X-ray beamline

system is defined as follows: X-axis corresponds to the direction of the X-ray beam; Z-axis points upward; Y-axis is in the horizontal plane, perpendicular to both X and Z, forming a right-hand-coordinate system with them. In the following subsections, we explain components of our beamline in detail. Characteristics of each component are summarized in table 2.

3.1. X-ray Generator

The X-ray generator (RIGAKU RU-200) is equipped with a water-cooled rotary type X-ray target. Seed electrons are emitted from a thermally heated W-filament with the size of 1 × 10 mm^2. The electrons are accelerated by a high bias voltage (5–20 kV), and finally hit target metals. The electrons hitting the targets are loosing their kinetic energy by the bremsstrahlung, line X-ray emissions characteristic to the target metals, and the heat. The surface of the target is tilted by 6° with respect to the beam direction. Hence the effective filament size looked at from the downstream side of X-rays is 1×1 mm^2. Currently we can choose Al, Ti, Cu and Pt as target metals, whose emission line appears at 1.49 keV (Kα), 4.51 keV (Kα), 8.04 keV (Kα), and 9.40 keV (Lα), respectively. A high rotation rate (6000 rpm) of the target and a water-cooling system enable us to obtain a high surface brightness of X-rays.

Table 2. Performance of the X-ray beam line.

• X-ray generator(Rigaku RU-200)	
Bias voltage	$5 - 20$ kV
Plate current	$10 - 200$ mA
Effective filament size	1×1 mm ^{2}
Target material	Al,Ti,Cu and Pt
• Vacuum tube	
Length	30 m
Diameter	31.5 cm
Pressure	$\sim 10^{-5}$ torr
• X-ray beam characteristics	
X-ray energy	$0.2 - 10$ keV
Beam size	> 0.2 mm
Beam divergence	> 1.6 arcsec
Beam stability	$\sim 1\%$(1 h after ignition)
• Stage strokes	
Sample chamber	
X (manual)	25 mm
Y	630 mm
Z	420 mm
θ_X	$\pm 180°$
θ_Y	$-5.5° \sim +4.9°$
θ_Z	$-4.2° \sim +4.7°$
Detector chamber	
X	210 mm
Y	660 mm
Z	420 mm

Table 3. Efficiencies of the detectors at Al, Ti, and Cu Kα line energy.

Energy	Efficiency[%]	
[keV]	PC	CCD
1.49 (Al)	12.6	18.0
4.51 (Ti)	75.0	54.0
8.04 (Cu)	29.6	14.3

3.2. Movable Slit

In order to simulate a real situation of observing celestial X-rays in orbit, a high parallelism is necessary for the X-ray beam. For this purpose, we use a movable slit 30 m away from the X-ray generator, in order to collimate the intrinsic dispersive X-ray beam.

In Fig. 5, we show a schematic view of the movable slit. The movable slit is actuated by three stepping motors which control the size of the window in the Y and Z directions ("slit-width" and "slit-height"), and the center position of the window in the Y direction ("slit-center") The height of the window center is adjusted to the level of the W-filament when the beam line was constructed. The widths can be as small as 0.2 and 0.5 mm in the Y and Z directions, respectively. Adopting a window size of w, we can obtain the X-ray beam with a full diverging angle ($\Delta\theta$) of

$$\Delta\theta = \arctan\left(\frac{w}{30\mathrm{m}}\right) = 6''.6\left(\frac{w}{1\mathrm{mm}}\right), \quad (1)$$

which is several times smaller than the core size of the image (see §§ 4.3).

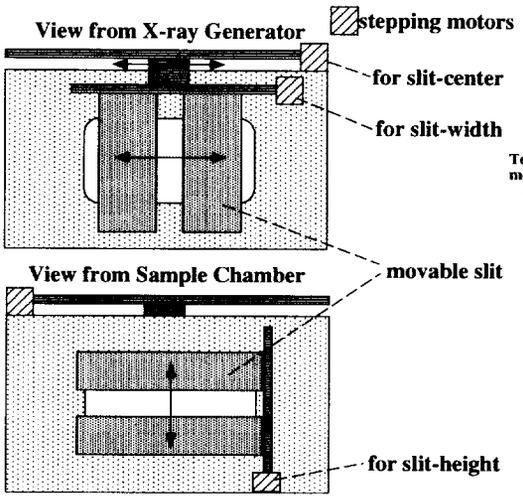

Figure 5. Schematic view of the movable slit. It can collimate the beam as small as 0.2 and 0.5 mm in Y and Z direction, and change the center of the beam in Y direction.

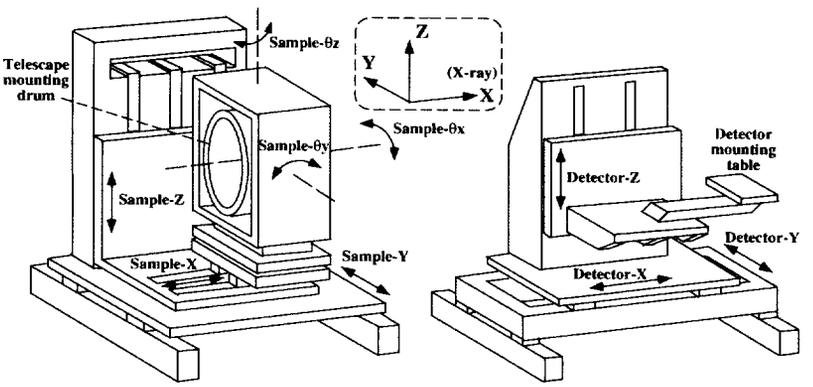

Figure 6. Specification of the mechanical stages in the sample (left) and the detector (right) chambers

3.3. Mechanical Stages

In order to fully illuminate the XRT with the narrow X-ray beam described above, we need to move the XRT in the evacuated sample chamber. Note that the detector should move simultaneously with the XRT for collecting the reflected photons. For this purpose, we have mechanical stages in both the sample and the detector chambers.

In Fig. 6, we show schematic views of the mechanical stages in the sample and detector chambers. The stroke of each stage is summarized in table 2. Both stages can move in the Y and Z directions. The detector stage can also move in the X direction to adjust the distance between the XRT and the detectors. The X stage in the sample chamber is moved manually. Its stroke, 25mm, corresponds to the difference between the focal lengths of the XRT–I and the XRT–S. In addition, we have triaxial rotational stages for the sample chamber stage. Among them, the rotational stages around the Y and the Z axes (hereafter referred to as θ_Y and θ_Z stages, respectively) are used for off-axis measurements.

3.4. Focal Plane Detectors

Two kinds of detectors, proportional counter (PC) and charge coupled device (CCD), are currently available in the ISAS X-ray beamline.

3.4.1. Proportional Counter

The proportional counter is operated by flowing P10 gas (90 % argon and 10 % methane) at 1 atm. The entrance window is a circle with 12 mmϕ covered with the aluminum-coated Mylar film with a thickness of 15 μm. We use a tungsten wire with 50 μmϕ for the anode. The depth of the gas measured from the entrance window is 22 mm. Note that PC has no imaging capability, and is mainly used to measure the total effective area of the XRT.

3.4.2. Charge Coupled Device

The charge coupled device, S5466, developed by Hamamatsu Photonics is adopted in the ISAS beamline. It has a 512×512 array of pixels, and the size of each pixel is 24 μm. It can thus cover 8.9×8.9 and 9.4×9.4 arcmin^2 for the XRT–I and the XRT–S, respectively. A saturation level of each pixel is ~300,000 electrons, and the averaged dark current is 3 e^-/pix/sec at the operation temperature of −50°C. S5466 is a frame transfer type CCD whose readout time is 2 sec. The exposure time can be controlled down to 20 ms with a mechanical shutter. All the command generations and data and status acquisitions are totally managed by the CCD controlling unit, C4880, also developed by Hamamatsu Photonics (Fig. 7).

In table 3, we tabulate the efficiencies of each detector at Kα line energies of Al, Ti, and Cu. In real measurements, we use monochromatic X-ray beams. We therefore use CCD in so-called "flux" mode in which the number of electrons generated by X-ray radiation is counted. The efficiency of the CCD in this table is for the flux mode.

3.5. System Operation

In Fig. 7, we summarize the system operation diagram of the ISAS beamline. The entire

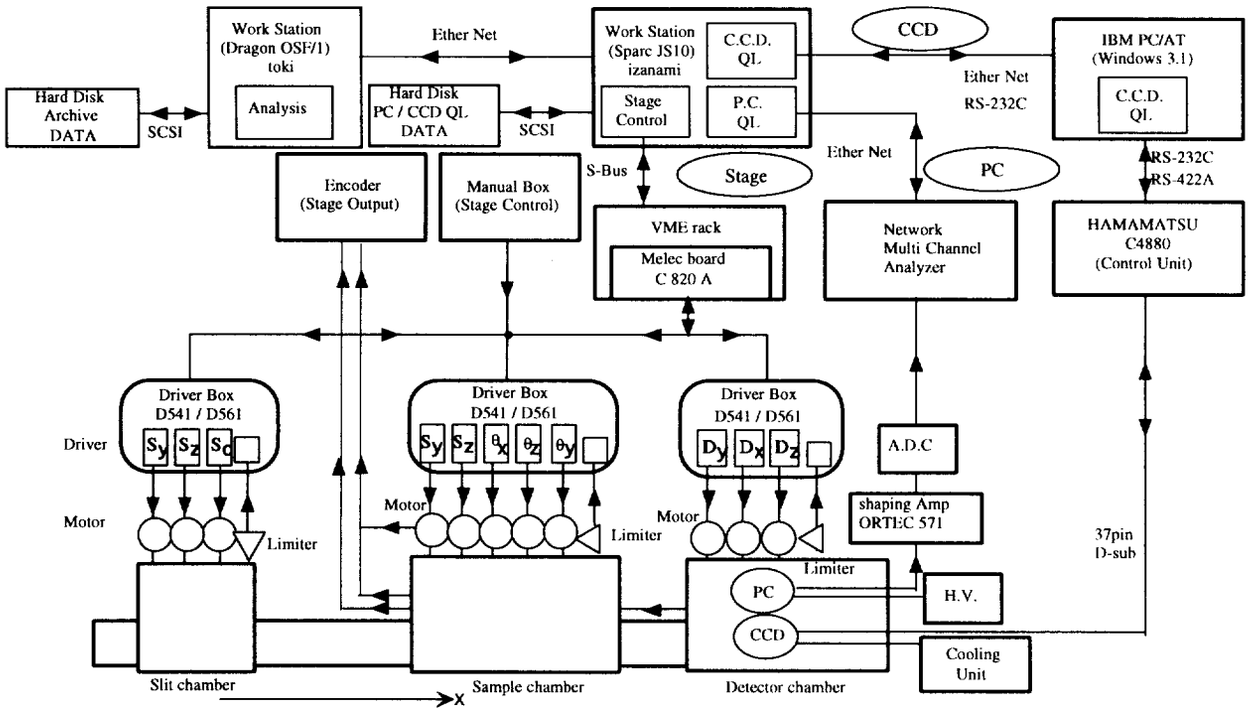

Figure 7. System operation diagram of the ISAS X-ray beamline.

system is controlled by a Spark JS10 (SunOS 4.1.4) work station, which generates commands to all the stages and receives status data from them. It also create data-acquisition commands for the PC and CCD through ether net and RS-232C, respectively, and collects data from them through ether net. The CCD system can be used as a stand alone system controlled by an IBM PC operated with Windows 3.1. In addition to these measurement system, we have another work station, DEC OSF/1, for the real time data analysis.

4. RESULTS OF PRE-FLIGHT CALIBRATIONS

In this section, we describe first results from the pre-flight calibration of the XRT–I carried out in the ISAS beamline. We have measured the effective area, the imaging capability, and the stray light at the energies of Kα lines of Al (1.49 keV), Ti (4.51 keV), and Cu (8.04 keV). As recognized from the designed effective area (Fig. 9), there is a huge discontinuity in the effective area at $\sim$ 2.2 keV. which corresponds to gold M shell (Au-M) absorption edge. The X-ray energies of Al-Kα (1.49 keV) and Ti-Kα (4.51 keV) are of great use in calibrating this discontinuity. On the other hand, Cu-Kα emission line (8.04 keV) is important in providing a data point in the energy range where the effective area decreases steeply with increasing X-ray energy.

4.1. Measurements of the Effective Area and the Imaging Capability

As mentioned in §§ 3.2, we collimate the intrinsic X-ray to obtain a highly parallel X-ray beam. In order to fully illuminate the XRT, we adopt the raster scan method: The sample Y stage and the detector Y stage (hereafter referred to as S_Y and D_Y stages, the same for the Z stages) are moved simultaneously from one edge of the XRT to the other. The detector collects reflected X-ray photons during this simultaneous Y scan. After this Y scan is finished, S_Z and D_Z stages are operated to shift both XRT and the detector by the beam width in Z direction. Then, S_Y and D_Y stages move in the opposite direction. These processes are repeated until the entire XRT face is illuminated.

In the case of using CCD, we use an X-ray beam size of 2×2 mm^2 in Y and Z with the movable slit. In this case, the full beam diverging angle is $13''$ (eq.(1)). On the other hand, the PC has no imaging capability and hence a larger beam size is allowable. We thus expand the size of the beam in Z direction to be 4 mm, which makes the time necessary for the full scan shorter.

In Fig. 8, we show the brightness distribution of the X-ray beam of Cu (8.04 keV) in the case of 2×2 mm^2 (for CCD). After removing Poissonic noise, the brightness distribution is flat within

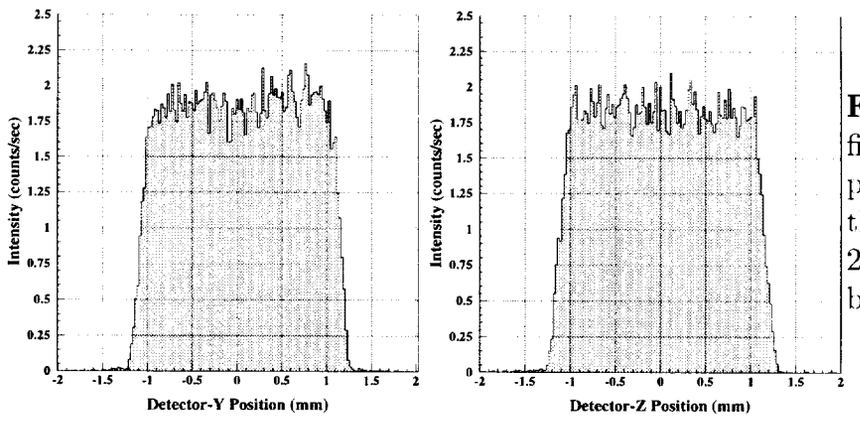

Figure 8. The X-ray beam profile with the size of 2×2 mm^2 projected on Y and Z axes. Note that the beam size is larger than 2 mm at the detector position because of the divergence.

a few percent. In order to use the CCD in the flux mode, it is important to make monochromatic X-ray beams. For this, we basically use a metal filter appropriate for each target. In table 4,

we summarize the set up of the X-ray generator, filters, and monochromaticity for each target. The monochromaticity of aluminum is somewhat worse than the others. This is the result of

Table 4. Set up of the X-ray generator, filters, and monochromaticities for the X-ray targets.

Target	Kα energy [keV]	High Voltage [kV]	Current [mA]	Filter Material	thickness [μm]	monochromaticity [%]
Al	1.49	6	20	Al	15	77
Ti	4.51	10	10	Ti	50	91
Cu	8.04	15	10	Ni	40	86

contamination by the continuum bremsstrahlung above ~4.5 keV, which cannot be removed by the filter completely. We have, however, confirmed that the resulting effective area and the imaging capability are both unaffected, if we change the high voltage of the X-ray generator to 10 kV. Hence the contamination above 4.5 keV is negligible.

4.2. Effective area

The effective area (S_{eff}) is defined to be the real photon-collecting area, and can be denoted as $S_{eff} = \bar{R} \cdot S_{geo}$, where $\bar{R}$ and S_{geo} are the average reflectivity over all the reflectors and the geometrical area of the XRT, respectively. $\bar{R}$ is the ratio of the number of photons detected during the raster scan over the entire XRT (C_{acc}) to the number of photons having illuminated the geometrical area of the XRT (C_0). If the scanning speed during the exposure is v, the beam width in Z direction (= step of the raster scan) is Δz, and the beam intensity per unit area is I, we obtain $C_0 = I \cdot (S_{geo}/v\,\Delta z)$. Therefore, the effective are can be written with only the system parameters and the measurable quantities as

$$S_{eff} = \frac{C_{acc}\, v\, \Delta z}{I}. \tag{2}$$

The effective area per quadrant was obtained based on the raster scan measurements with the PC and the CCD at the three Kα energies, according to eq.(2). The results from both detectors are consistently within 1 % at all the energies. Table 5 summarizes the resulting effective areas per XRT-I measured at the boresight (= on-axis). They are 460, 313, 250 cm^2

Table 5. Effective area of ASTRO-E XRT–I

Photon Energy	[keV]	1.49	4.51	8.04
Effective Area	[cm^2]	460 ± 1	313 ± 1	250 ± 1

per XRT–I at 1.49, 4.51, and 8.04 keV, respectively. Note that it is found from the analysis of the image (§§ 4.3) that more than 98% of all the reflected photons are within the FOV of both the PC and the CCD. The measured effective areas are also shown in Fig. 9 together with the ideal effective area calculated based on the XRT design parameters. For comparison, ASCA

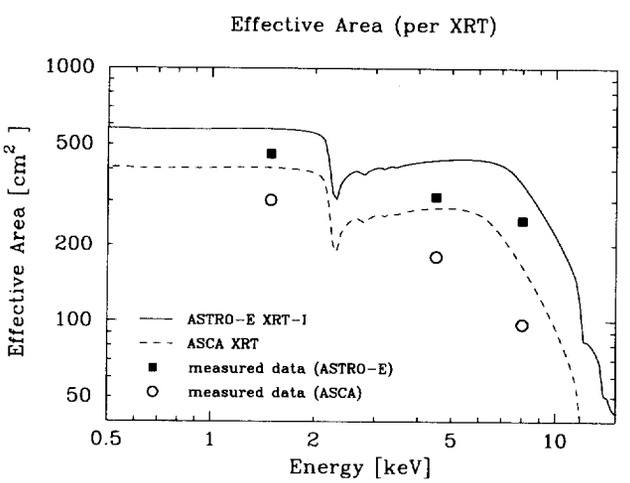

Figure 9. On-axis effective area of each XRT–I and ASCA XRT against X-ray energy. Marks are measured values, and the curves are the ideal effective areas calculated based on the XRT design parameters. The sharp drop at about 2.2 keV is attributed to the gold M-edge complex.

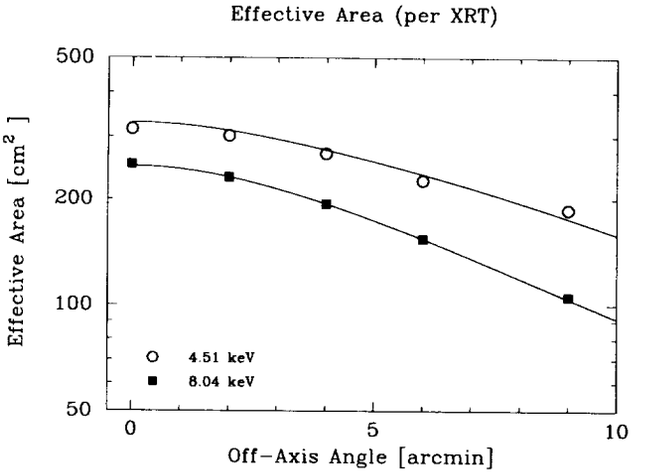

Figure 10. Angular response of the effective area at 4.51 and 8.04 keV. The effective area gradually decreases with the off-axis incidence because of neighboring reflectors shadowing and the increase of the average incident angles (vignetting). Curves are empirical model functions (double Gaussian). Marks are measured values.

XRT values are also shown. The ideal effective area assumes that the reflector has no surface roughness and that the placement of the reflectors is perfect. From this figure, it is recognized that the measured values of both XRT–I and ASCA are $\sim$ 75–80 % of ideal effective areas. In a separate experiment, we measured the reflectivity of each reflector and found that it is close to the ideal. Therefore, we consider that the smaller effective area is probably due to a slight misalignment of the reflectors. The measured effective areas of XRT–I are larger than the ASCA XRT by a factor of 1.5 and 2.5 at 1.49 and 8.04 keV, respectively.

The effective area is a function of the incident X-ray angles as well as the incident X-ray energy. Figure 10 shows the angular response of the effective area at X-ray energies, 4.51 and 8.04 keV. The abscissa indicates the "off-axis angle" which is the angle between the directions of incident X-rays and the XRT optical axis (= symmetry axis). One of the appropriate empirical models for the angular response is found to be a two Gaussian model, which is also drawn in the figure. The effective area drops with the off-axis angle because the neighboring reflectors prevent X-rays passing through and the reflectivity decreases more sensitively to the off-axis angle in higher X-ray energies. This is the so-called "vignetting effect." The field of view of the XRT–I, which we define to be the off-axis angle at which the effective area becomes half of the on-axis value, is $20'\phi$ and $15'\phi$ at 4.51 and 8.04 keV, respectively.

4.3. Image quality

The image quality of the XRT–I has been measured by the raster scan method using the CCD with a 2 $\times$ 2 mm^2 X-ray beam (13 arcsec beam divergence). Currently the measurement has

been done only at Ti-Kα energy (4.51 keV). Figure 11 shows the on-axis image of the XRT–I by logarithmic scales of contours. Since the positioning of reflectors close to the boundaries

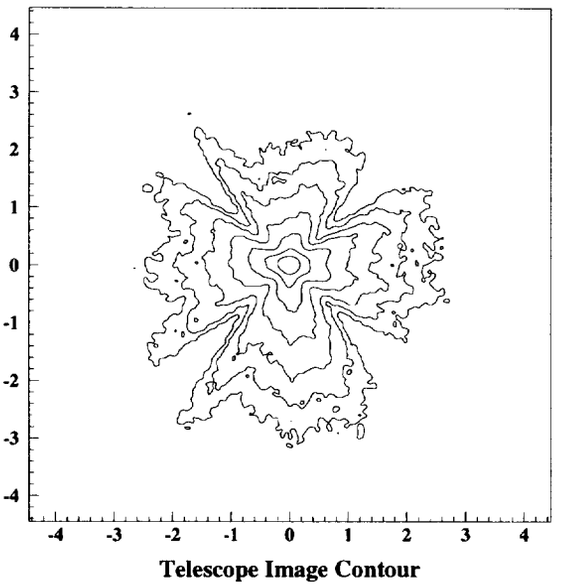

Figure 11. The XRT–I on-axis image at 4.51 keV. Contour levels are logarithmic, and 0.006, 0.012, 0.026, 0.054, 0.113, 0.237, 0.497 times of the peak flux.

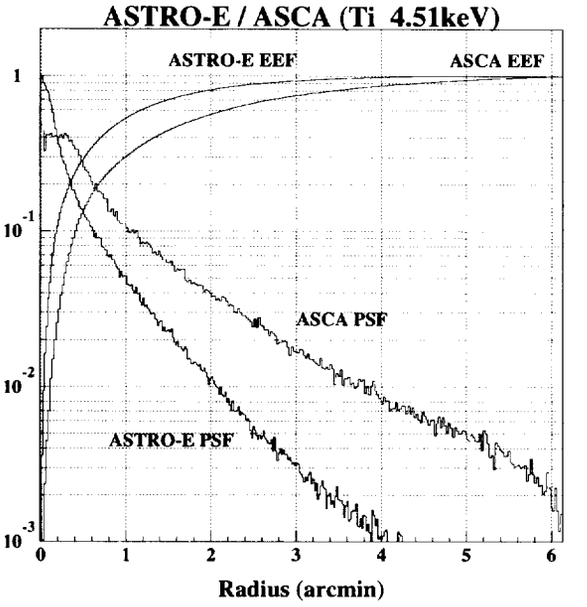

Figure 12. Point Spread Function (PSF) and Encircled Energy Function (EEF) of ASTRO-E XRT compared with ASCA-XRT.

of the quadrant are relatively poorer, degrading the image quality, the area of XRT between the housing side walls and the first alignment bars are masked before setting up the XRT into the sample chamber. As a result, the image is not circular, but four butterfly-like wings are seen. It is recognized from Fig. 11 that the core of the image is very sharp, and the surface brightness drops to one-half and to 1 % of the peak at the radius of only 0.2 and 2 arcmin, respectively. This situation is more quantitatively shown in Fig. 12. In this figure, the point spread function (PSF) is the surface brightness of each CCD pixel as a function of the radius averaged azimuthally. For comparison, we have also shown the ASCA XRT PSF. Both PSFs are normalized by the number of accepted photons by the same CCD, and renormalized so that the PSF of the XRT–I becomes unity at the image center. PSF of the XRT–I has a sharper core and smaller amount of an exponential scattering tail. Both are benefits of the replication method of the reflector production (§§ 2.2). The former is the result of a reduction of undulation with a length scale of several tens down to several mm, and the latter is brought about by a reduction of the surface roughness with the scale down to several μm. From the evaluation of the scattering tail, we have found that more than 98 % of the reflected photons are within the $8.9' \times 8.9'$ field of view of the CCD.

In Fig. 12, the encircled energy functions (EEF) of the XRT–I and the ASCA XRT are shown. EEF is the fraction of the number of reflected photons coming within a certain radius. The diameter at which EEF becomes 0.5 is usually referred to as the half power diameter (HPD),

and conventionally is used as one of the quantitative expressions of the imaging capability. HPD of the XRT–I is obtained to be 1.84±0.04 arcmin, which is two times better than the ASCA XRT. Note that the normalized radii of EEFs are 4.5 arcmin and 6.0 arcmin, respectively, for the XRT–I and the ASCA XRT because we use the same CCD for both in spite of the difference of the focal lengths (4750mm and 3500mm: see the plate scale in table 1).

4.4. Stray Light

Because of the thin reflector-nesting configuration of the XRT, it is possible that X-rays intrude from outside the field of view (FOV). In Fig. 13, we show patterns of the stray lights. The

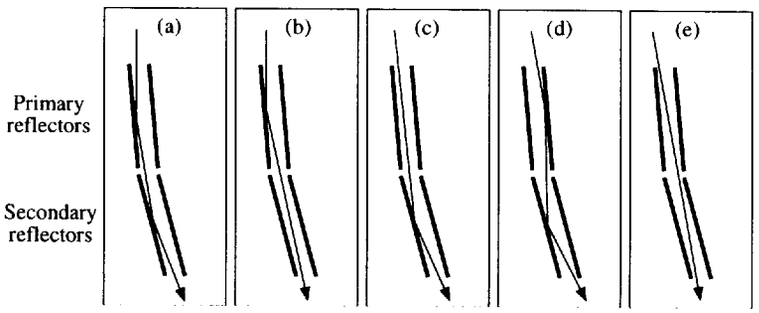

Figure 13. Four examples of XRT light paths: (a) normal path, (b) reflection only by primary reflectors, (c) reflection only by secondary reflectors, (d) multiple reflections by front and back surface of reflectors, (e) direct path (no reflection).

normal light path is (a), and the others are the stray lights. They are classified as (b) primary reflection, (c) secondary reflection, (d) multiple reflection, and (e) no reflection. Among them the multiple reflection is expected to have an energy dependence, because it includes reflection at the backside of the reflector which is bare aluminum. The multiple reflection is thus expected to be more intense for lower X-ray energies.

Since the stray lights spread widely over the focal plane, we have performed a mosaic mapping with the CCD. We set a sector of the XRT-I horizontally, and performed a one dimensional scan in Y direction with 2×2 mm^2 X-ray beam, simultaneously with the S_Y and the D_Y stages. In this configuration, the stray lights spread in the Y direction. Therefore, the CCD was moved in this direction with the D_Y stage for the mosaic mapping. The stray lights were measured at offset angles of 0.5° and 1.0° The XRT is rotated around the Z axis by these values by using θ_Z stage. The stray lights were measured at the X-ray energies of 1.49, 4.51 and 8.04 keV.

Figure 14 displays the one dimensional brightness distribution of the stray lights with the offset angle of 0.5° (panel (I), (II), and (III)) and 1.0° (panel (IV) and (V)). The ordinates are the brightness (counts s^{-1} mm^{-2}) in the focal plane in the case when the X-ray star with the on-axis intensity of 1 count s^{-1} is the source of the stray lights. Note that the on-axis position of the XRT–I is 30′ in the abscissa for the upper three panels, and 60′ for the lower two panels.

As noticed from this figure, the on-axis position (at which the detector locates in orbit) is contaminated by two components of the stray light, (c) secondary reflection and (d) multiple reflection. As expected, the multiple reflection component decreases with increasing X-ray energy, and becomes almost negligible at Cu-Kα and Ti-Kα energies (8.04 keV and 4.51 keV) for the off-axis angles of 0.5° and 1.0°, respectively. Note that the peak brightness of the stray light at Al-Kα (1.49 keV) is only 2×10^{-5} counts s^{-1} mm^{-2} (component (c)), which is almost

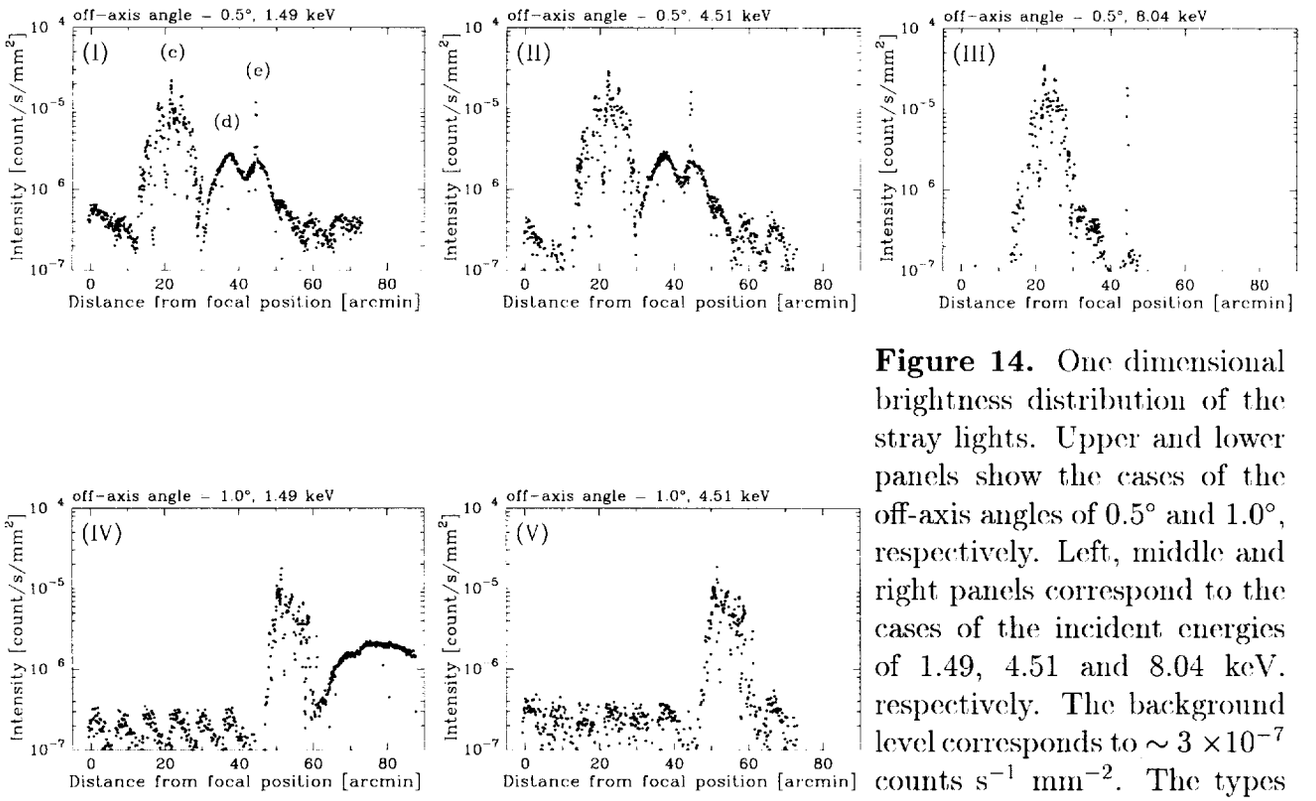

Figure 14. One dimensional brightness distribution of the stray lights. Upper and lower panels show the cases of the off-axis angles of 0.5° and 1.0°, respectively. Left, middle and right panels correspond to the cases of the incident energies of 1.49, 4.51 and 8.04 keV. respectively. The background level corresponds to $\sim 3 \times 10^{-7}$ counts s^{-1} mm^{-2}. The types of the stray lights are indicated in the top left panel in relation with Fig. 13.

the same as the ASCA XRT. However, the intensity of the multiple reflection is several factors smaller than ASCA.

5. SUMMARY AND CONCLUSION

We have been measuring the properties of ASTRO-E XRT–I. at the ISAS 30 m beam facility. We have obtained the effective area to be 460, 313, and 250 cm^2 per XRT at the incident X-ray energies of 1.49, 4.51, and 8.04 keV, respectively. The larger geometrical area of the XRT brings about an energy-independent increase of the effective area by a factor of $\sim$ 1.5. The longer focal length makes the incident angles of the primary reflectors smaller, which leads to a further increase of the effective area at higher energies. Resultingly, the effective area of the XRT–I becomes significantly larger than that of ASCA by a factor of 1.5 and 2.5 at 1.49 keV and 8.04 keV, respectively. The difference between the measured values and the ideal effective area curve is probably caused by the slight misalignment of the reflectors.

The point spread function obtained from our sample image has a very sharp core and a small exponential scattering tail. The half power diameter was obtained to be 1.84 arcmin at 4.51 keV, showing a better focusing capability than ASCA by a factor of 2, owing to the advanced reflector production technique. The sharp core is the result of reduction of undulation

with a length scale of several tens down to several mm, and the small scattering tail was brought about by reduction of the surface roughness with scale down to several μm.

The brightness of the stray light was obtained to be less than 2×10^{-5} counts s^{-1} mm^{-2} in the case when an X-ray star with the on-axis intensity of 1 count s^{-1} is the source of the stray lights. This peak brightness is caused by the secondary reflection, and hence it is almost the same as ASCA. However, the brightness of the multiple reflection component is remarkably smaller than ASCA, at least by several factors. This is the result because the backside of the reflector of ASTRO-E XRT is a bare aluminum; but it was coated by acrylic lacquer in the ASCA XRT.

REFERENCES

1. M. C. Weisskopf, S. L. O'Dell, R. F. Elsner, and L. P. Van Speybroeck, *Proc. SPIE*, **2515**, pp.312-329, 1995.
2. D. H. Lumb, H. Eggel, R. Lainé, and A. J. Peacock, *Proc. SPIE*, **2808**, pp.326-337, 1996.
3. J. v. Casteren, *Proc. SPIE*, **2808**, pp.338-349, 1996.
4. P. Serlemitsos et al, *Publication of Astronomical Society of Japan*, **47**, pp.105-114, 1995.
5. Y. Soong et al, *Proc. SPIE*, **2515**, pp.64-69, 1995.
6. P. Serlemitsos et al, *Astrophysics & Space Astronomy*, **239**, pp.177-196, 1996.